ELSEVIER

Biophysical Chemistry 121 (2006) 30 – 43

Biophysical Chemistry

http://www.elsevier.com/locate/biophyschem

Mechanism of β-purothionin antimicrobial peptide inhibition by metal ions: Molecular dynamics simulation study

Svetlana Oard [a,*], Bijaya Karki [b]

[a] LSU AgCenter Biotechnology Laboratory, Louisiana State University, 115 Wilson Building, LSU, Baton Rouge, LA, 70803, United States
[b] Department of Computer Science, Louisiana State University, Baton Rouge, LA, 70803, United States

Received 9 October 2005; received in revised form 7 December 2005; accepted 7 December 2005

Abstract

Wheat β-purothionin is a highly potent antimicrobial peptide which, however, is inactivated by metal ions. The key structural properties and mechanisms of inhibition of β-purothionin were investigated for the first time using unconstrained molecular dynamics simulations in explicit water. A series of simulations were performed to determine effects of temperature and the metal ions. Analyses of the unconstrained simulations allowed the experimentally unavailable structural and dynamic details to be unambiguously examined. The global fold and the α1 helix of β-purothionin are thermally stable and not affected by metal ions. In contrast, the α2 helix unfolds with shift of temperature from 300 K and in the presence of metal ions. The network of conserved residues including Arg30 and Lys5 is sensitive to environmental changes and triggers unfolding. Loop regions display high flexibility and elevated dynamics, but are affected by metal ions. Our study provides insights into the mechanism of metal ion-based inhibition.

Keywords: Antimicrobial activity; Antifungal activity; Mechanism of inhibition; Metal ions; Molecular dynamics simulations; β-Purothionin

1. Introduction

β-purothionin (βPTH), found in the endosperm of wheat, belongs to a group of highly basic, cysteine-rich plant peptides, thionins. βPTH displays a broad spectrum of antibacterial and antifungal activity which is significantly higher than for melittin or cecropin B [1–3]. Experimental data suggest that βPTH inserts into the hydrophobic core of the lipid bilayers and significantly modifies the lipid packaging at the surface of the bilayer increasing the accessibility of water molecules [4,5]. The tertiary structure of βPTH is key to the important property of membrane disrupting capability in a wide range of microbial cells. The three-dimensional structure of β-purothionin has been solved by X-ray diffraction [6]. The molecule is divided into a stem formed by two antiparallel α-helices and an arm formed by a coil in extended conformation, b-turns T1 and T2, and an antiparallel β-sheet consisting of two β-strands. The global structure is stabilized by four disulfide bonds with two bonds connecting the stem and another two bonds connecting the arm. The arm and stem are connected by hydrogen bonds and salt bridges forming the tertiary structure which resembles the Greek letter gamma (Γ) [4].

Available experimental results on βPTH provide a good starting point for further investigations to elucidate a mechanism of membrane permeabilization. Thus, thermal denaturation experiments were reported for the thionin from *Pyrularia pubera* and its D32R analog [7]. It has been shown that helicities are fully preserved between 5 and 80 °C, and the D32R mutation decreases helical content. In addition, mono- and divalent metal ions interfere with interactions of thionins with phospholipid vesicles and membranes. Thus, 2–5 mM Ca^{2+} completely blocks activity of thionin, although 50 mM concentrations of monovalent ions like Na^+ and K^+ are necessary for inactivation [1,8]. A highly conserved Tyr13 residue was proposed as an essential component for plasma membrane disruption [4,9,10].

Abbreviations: ahRMSD, RMSD for all heavy solute atoms; bbRMSD, RMSD for backbone heavy solute atoms; MTS, multiple-time-scale; βPTH, β-purothionin; βPTH-300K, the MD trajectory without metal ions at 300 K; βPTH-K, the MD trajectory in the presence of 100 mM K^+ ions at 300 K; βPTH-Mg, the MD trajectory in the presence of 20 mM Mg^{2+} ions at 300 K.

* Corresponding author. Tel.: +1 225 578 7865; fax: +1 225 578 7863.
E-mail address: soard@agctr.lsu.edu (S. Oard).

0301-4622/$ - see front matter © 2005 Elsevier B.V. All rights reserved.
doi:10.1016/j.bpc.2005.12.004

A consensus Arg30 is thought to be involved in charge-based interactions with the membrane [7,11]. However, the mechanisms of membrane disruption and cation inhibition of membrane disrupting activity of thionins are not known.

Investigations of βPTH properties and cation inactivation of the peptide are critical for understanding a membrane-permeabilizing mechanism and for developing effective antimicrobial agents. We used unconstrained explicit solvent molecular dynamics (MD) simulations to elucidate effects of temperature and metal cations on βPTH structure and dynamics to understand the mechanism of metal cation-based inhibition of thionins. Advances in computer science enabled application of methodologies developed for material science to study biomolecules [12–14]. We focused on accuracy of MD computations to adequately represent the experimental model and to make reliable predictions of peptide properties. Because accuracy of MD calculations depends on a number of simulation parameters [15–17], special care was taken to determine an optimal set of parameters for the model system, insuring accurate computations of electrostatic and van der Waals (VDW) interaction energies. The relatively small size of βPTH and use of the massively parallel computer cluster allowed us to achieve the nanosecond timescale without compromising computational accuracy. Our computational model in fact produced results comparable with the experimentally observed data. Calculated MD trajectories at different environmental conditions shed light on new details of βPTH properties and the mechanism of metal ion inhibition of βPTH membrane permeabilization activity.

2. Computational methods

2.1. Molecular model

The initial structure of βPTH from wheat seed was obtained from the X-ray structure of Stec et al. [6], determined at 1.7 Å and pH 5.9, with a PDB entry code 1BHP. All water and ligand molecules determined by crystallography were removed. The coordinates of hydrogen atoms were then generated using the MKMOL function of Peach 5.8 [18] and minimized. Since a solvent model is essential for obtaining meaningful results in the presence of metal ions, the flexible, single point charge (fSPC) water potential was chosen for this study [19]. βPTH was solvated in a cubic periodic boundary box of the fSPC water [20]. The width of the box was set to 12 Å from the border of the solvent-accessible surface. To neutralize the overall charge of the peptide, the chloride ions were added to the simulation box by replacing water molecules so that the peptide-ion electrostatic interaction would be at a minimum. The final solvated system consisted of one molecule of β-purothionin (685 atoms), 9 chloride ions, and 4492 H_2O molecules resulting in 14,170 total atoms.

2.2. Computational methodology

Atomic parameters used to describe all atoms were taken from the Amber99 force field library [21]. The Peach 5.8 software package for MD simulations of biological molecules [18,22,23] was applied to investigate βPTH. The MD simulations were carried out in periodic boundary conditions and the canonical ensemble using the Nose–Hoover thermostat [24,25]. No bond length constraints were applied in this study to investigate βPTH properties using MD simulations which are as "natural" as possible. Simulations were run with the multiple-time-scale (MTS) method [22]. The long-range Coulomb forces were calculated using the particle mesh Ewald method [26]. The neighbor atom lists were upgraded every 10 steps. The Peach 5.8 code was run in parallel mode on Intel Xeon-based Linux cluster SuperHelix with Myrinet network.

Each simulation box was pre-equilibrated before performing MD simulations. The ions and water were subjected to minimization and heating to 300 K as described elsewhere [27] while holding all peptide atoms rigid. Ions and water were pre-equilibrated by running canonical MD simulations for 1 ns at 300 K to allow optimal positioning around the peptide. Next, all atoms were allowed to move, and the system was minimized for 100 steps and then heated to a desired temperature as described above.

To study evolution of the molecular structure and stability, βPTH was simulated for 2 ns at 300 K. Computer simulations can provide atomistic details interpreting experimental results, in particular study of structural properties as a function of temperature [28]. The temperature dependence of the structure stability was analyzed at 280, 360, and 400 K with all other conditions kept the same. Interactions of the peptide with metal ions were simulated at 300 K in the presence of 100 mM K^+ ions or 20 mM Mg^{2+} ions [1,7]. To reach corresponding concentrations, the 9 K^+ or 2 Mg^{2+} ions were added to the simulation box with βPTH, and the chloride ions were added proportionally to neutralize the system. The simulation boxes were prepared starting from the X-ray structure as described above.

2.3. Optimizing simulation parameters

We determined the optimal set of simulation parameters to achieve desirable levels of accuracy for our model. The accuracy test for a time step was performed using 500-step microcanonical MD runs at 300 K initial temperature. The single time step method was compared with the MTS method which divides interactions into three subsets of soft (bonded), medium (non-bonded VDW and for $(i,j)=1–4$ pairs), and hard range forces (electrostatic) calculated with time steps Δt_s, Δt_m, and Δt_h, respectively. A 12 Å cutoff for VDW and short-range electrostatic interactions and the Ewald sum parameter eta of 4.8×10^{-5} were applied in this test. The evaluation of the stability of the integration was performed by computing the relative root mean square fluctuation ($RMSF_r$) of the total energy for a trajectory [22]. Sufficient accuracy with average $RMSF_r$ of total energy $\leq 0.1\%$ was achieved using the MTS method with the time step scheme 4.0, 1.0, and 0.25 fs for Δt_s, Δt_m, and Δt_h, respectively (see Supplementary Material, Table 1). The implementation of the MTS method for our model system allowed a 12-fold decrease in the central processing unit

(CPU) time used to compute a femtosecond of the simulation. The effects of the Ewald summation parameters, cutoff and eta, on calculations of VDW and short-range electrostatic interactions in terms of convergence of total energy for our system were tested using 5000-step microcanonical MD runs with the selected MTS scheme. The best compromise between accuracy and CPU usage was observed with a 15 Å cutoff and a 4.8×10^{-5} eta (see Supplementary material, Table 2). These values resulting in a desirable level of computational accuracy with the total energy error below 0.1% were adopted for canonical MD simulations. The test of computational scaling of the Peach 5.8 code for our system allowed us to identify parallel efficiency and time performance for MD simulations with the identified set of parameters (data not shown). The best parallel efficiency/time performance corresponded to 16 dual-node processors of SuperHelix with ~47 CPU h required for computing a 1-ns long simulation.

2.4. Analysis

Analysis of the MD trajectories was performed using Peach 5.8 [18] and Amber 8 [29]. Convergence of MD trajectories was assessed by averaging all heavy solute atom RMSD values for all heavy solute atoms from the initial structure over 100-ps intervals. The conformational dynamics of the generated trajectories were analyzed by computing root mean square difference (RMSD) for all heavy atoms (ahRMSD), backbone N, Cα, and C′ atoms (bbRMSD), and side chain atoms (scRMSD) of the solute and root mean square fluctuation (RMSF). The RMS fluctuation around the time averaged structure was computed for each amino acid residue to analyze the fluctuation pattern within the peptide. Average structures, residue RMSD, RMSF, average solvent-accessible area (SAA), and hydrogen bonds were determined from the last 400 ps or the second nanosecond of MD trajectories to analyze effects of temperature or metal ions, respectively. Secondary structures were defined with the DSSP program [30]. For visualization of structures and trajectories, the VMD1.8.3 [31] and MOLMOL 2K.2 [32] were used.

To calculate pK_a, the MD trajectories with K^+ and Mg^{+2} were superimposed on the MD trajectory at 300 K without cations. The same atomic partial charges and radii were used as in the MD simulations. Partial atomic charges used for the pK_a calculations were modified to neutralize residues ionized at pH 7 [33]. The pK_a shifts were calculated as described [34] with the electrostatic potential obtained using the Adaptive Poisson–Boltzmann Solver software package (http://mccammon.ucsd.edu/apbs). The electrostatic potentials were calculated as described [35].

3. Results and discussion

3.1. Structure and dynamics of βPTH at 300 K

To investigate structure and dynamics of βPTH, we performed the unconstrained MD simulation in explicit water at ambient temperature (βPTH-300K). The βPTH-300 K trajectory was structurally stable during the entire 2-ns period. The peptide reached the equilibrium within the first 600 ps as confirmed by averaging the backbone RMSD values and calculated radius of gyration (see Supplementary material, Fig. 1). After reaching the equilibrium, the RMSD from the starting crystal structure fluctuated around 1.2 Å for the backbone (bbRMSD) and 2.0 Å for all heavy atoms (ahRMSD) over the course of the simulation (Fig. 1B). The global fold of the MD structure maintained general features of the Γ [4,6]. The superposition of the crystal and MD structures displayed a nearly identical fit of the MD trajectory with all secondary structures and disulfide bonds showing nearly identical configurations (Fig. 1C). No significant structural and dynamic changes were found between 600 ps and 2 ns (Fig. 1D).

The βPTH-300K trajectory displayed new insights into structural and dynamic properties of βPTH in water. The ahRMSD and bbRMSD for the helices α1 and α2, and β-sheet with respect to the crystal structure demonstrate significantly smaller conformational differences for these secondary structures than for the L1 and L2 loops (Fig. 1E). In addition, residues of both helices and the β-sheet mainly display the small RMSF, which is a measure of mobility. The only exception is the N-terminus of the α2 helix with Gln23 largely fluctuating throughout the simulation. In contrast, both loops are the most flexible and dynamic regions in the peptide as indicated by the largest backbone RMSD and RMSF values. This finding is consistent with increased flexibility previously reported in loops [27,36]. However, the increased mobility in the loop regions observed in the PTH-300K trajectory does not agree with the temperature factors of the crystal structure [6] which suggest significantly higher mobility in the C-end of the α2 and Arg30 than in the loop regions. We show below, that the presence of Mg^{+2} ions causes similar changes in mobility of βPTH. βPTH crystals contained several ligands and were obtained by equilibration against the buffer containing 20% $MgCl_2$ [6] that explains differences in mobility observed in crystals and the PTH-300K trajectory.

The highly conserved residue Tyr13, situated at the inner corner of the Γ, remains buried in the peptide core throughout the entire simulation with the small RMSD and RMSF values. The other conserved residue Arg30 is positioned at the outer corner of the Γ. The side chain of Arg30 undergoes the largest displacement even though the backbone atoms are constrained by the neighboring disulfide bridges. However, the relatively small RMSF value indicates a stabilized conformation of the Arg30 side chain. We found that the Arg30 and Lys5 side chains, which are almost parallel to each other in the initial structure, bend in opposite directions during the simulation. Interestingly, proximity of these residues is insured by two disulfide bridges. Lys5, Arg30, and the surrounding cysteines are highly conserved and could be essential for antimicrobial activity [2,11].

The global Γ fold is supported by the hydrogen bonding network between Cys4, Lys45, Arg10, and Ser2 that connects the arm and the stem as in the crystal structure (Table 1). Lys45-O forms strong hydrogen bonds with Cys4-N and Agr10-NH2, Lys45-OT with Arg10-NE, and Ser2-OG forms with Arg10-

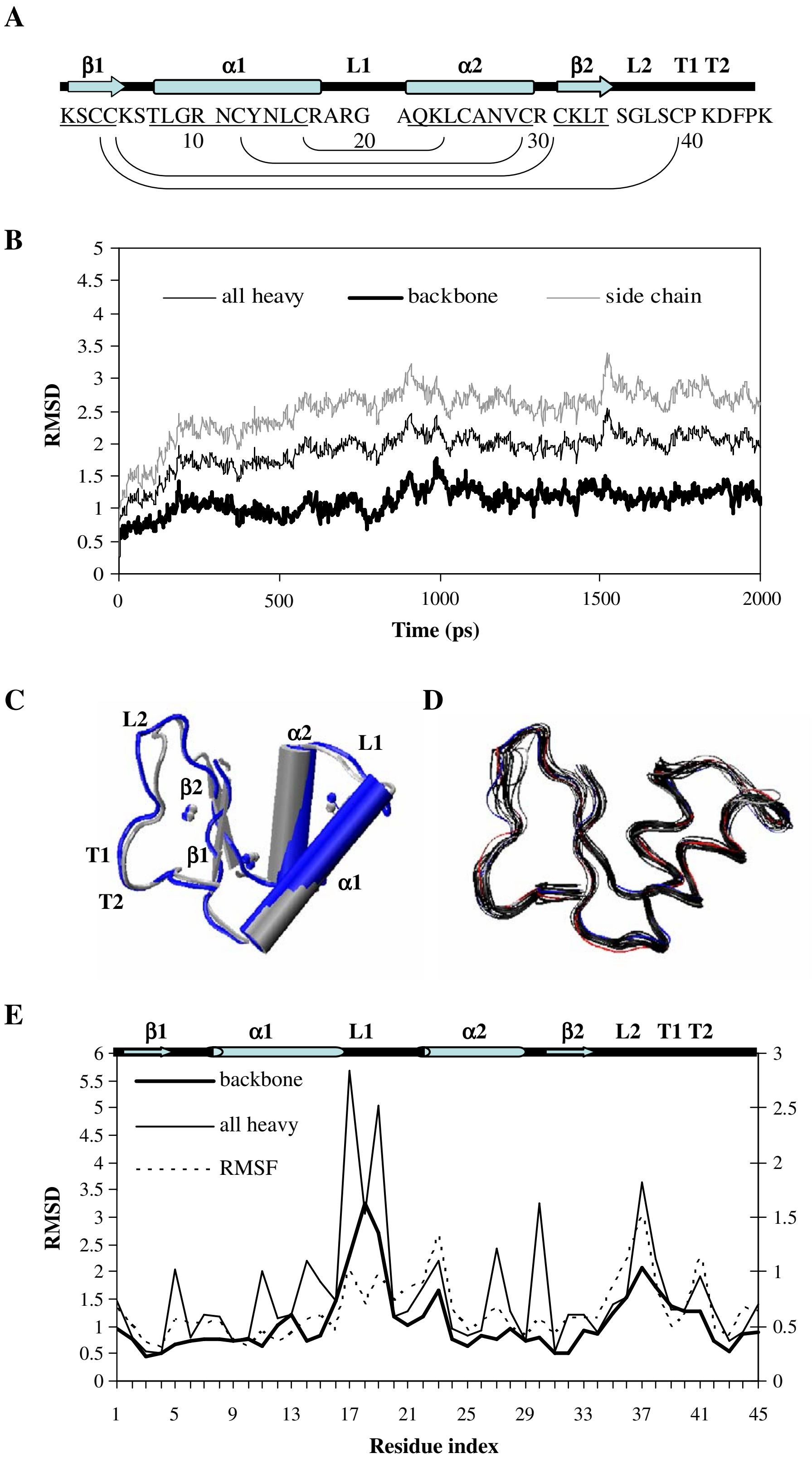

Fig. 1. MD simulation of βPTH in explicit water at 300 K. (A) Amino acid sequence of βPTH with secondary structure elements determined by X-ray crystallography [6] are shown above the sequence and underlined. The loops and b-turns are labeled L and T, respectively, and the disulfide bonds are shown by brackets. (B) Time evolution of RMS Deviations (in angstroms) between the MD trajectory and the crystal structure during the 2-ns simulation. RMSD for all heavy (black line), the side chain (gray line), and the backbone (heavy black line) atoms of the solute. (C) Superposition of the average MD structure at 300 K (black) with the crystal structure (gray) with the disulfide bonds shown as connected spheres. (D) Snapshots of the MD structures taken with 100-ps intervals between 600 ps and 2 ns. (E) RMSD and RMS fluctuations (in angstroms) as functions of residue indices. The ahRMSD (continuous line), the bbRMSD (heavy continuous line), and RMSF (dashed line) computed over the last nanosecond. Schematic representation of the secondary structure for the crystal structure is shown above the plot in correspondence with residue indices.

Table 1
Fraction of hydrogen bonds in MD simulations of βPTH at different conditions

Hydrogen bond		Distance	%[a]					
Donor	Acceptor	CrS[b]	280 K	300 K	360 K	400 K	300 K 100 mM K^+	300 K 20 mM Mg^{+2}
Cys4N	Lys45O	2.8	84	79	87	0	88	88
Cys4N	Lys45OT	Not present	0	0	0	70	0	0
Lys45N	Cys4O	2.78	66	78	66	64	89	90
Arg10NE	Lys45OT	2.87	98	79	90	0	88	89
Arg10NH2	Lys45O	2.92	82	79	76	36	89	90
Arg10NH2	Lys45OT	Not present	0	0	0	92	88	89
Arg10NH1	Ser2OG	2.92	64	80	0	44	89	88
Lys5NZ	Asp42O	Not present	0	82	72	64	37	74
Lys5NZ	Asp42OD2	Not present	0	28	0	0	99	80
Arg30NH1	Asn27O	Not present	18	81	0	0	90	89
Arg17NH2	Asn14OD1	Not present	60	81	0	0	0	0

[a] A hydrogen bond is considered if the donor–acceptor distance is smaller than 3 Å and the donor–hydrogen-acceptor angle is larger than 135°.
[b] Crystal structure [6].

NH1 the outer hydrogen bond of the Γ. A new hydrogen bonding cluster is found in βPTH-300K at the outer corner of the Γ involving two basic residues, Lys5 and Arg30 which are linked by disulfide bridges. Lys5 forms a hydrogen bond with Asp42, and Arg30 forms a Arg30-NH1:Asn27-O hydrogen bond. As we show below, these coupled hydrogen bonding interactions stabilize the Arg30 side chain in the βPTH-300K trajectory.

Thus, The MD simulations performed in this work for the first time elucidate details of the βPTH structure and dynamics. βPTH in water at the ambient temperature maintains the global Γ fold and all secondary structures which are nearly identical to the crystal structure. However, dynamics of the βPTH in water differ from those at the βPTH in crystals. Our MD simulations demonstrated that the α2 helix and Arg30 fluctuate significantly less while loop regions display higher fluctuations compared to the crystal structure. This difference may be explained by the fact that βPTH crystals contained several ligands and Mg^{+2} ions. The Γ fold is maintained by several strong hydrogen bonds similar to those of the crystal structure. The new hydrogen bonding network Asn27-Arg30-Lys5-Aps42 is found at the outer corner of the Γ in this study as well.

3.2. Thermal stability

Effects of temperature were analyzed in the 1-ns MD simulations at 280, 360, and 400 K. We used the AMBER (parm99) force field for these simulations as well because this force field was shown to satisfy the majority of experimental data within the temperature range of 280 to 400 K [37,38]. The equilibrium of the peptide in the βPTH-300K trajectory was achieved after 600 ps (see Supplementary material, Fig. 1). Therefore, 1-ns long MD simulations at different temperatures allowed us to assess thermal stability of secondary structures.

The time evolution of bbRMSD for MD trajectories calculated at different temperatures from the starting crystal structure is presented in Fig. 2A. Fluctuations of bbRMSD at 280 K were similar to that at 300 K. Elevation of temperature resulted in the accelerated increase of bbRMSD over the simulation time in comparison to bbRMSD at 300 K. This finding is consistent with previously reported high-temperature MD simulations of small proteins [39]. Interestingly, the bbRMSD values of the trajectories at 360 and 400 K increased similarly during first 300 ps, but later the bbRMSD values of the trajectory at 400 K decreased and approached bbRMSD of the βPTH-300K trajectory. Despite similarity of the final bbRMSD values at 280, 300, and 400 K, the peptide underwent considerable conformational changes with a temperature shift 300 K. Superposition of the MD structures obtained at the various temperatures demonstrates thermal stability of the global Γ fold (data not shown). However, secondary structures display different levels of thermal stability (Table 2). The β-sheet is temperature sensitive. The α1 is thermally stable and enlarges with shifts of temperature from 300 K in either direction. In contrast, the α2 helix is highly temperature sensitive and unfolds at both low and elevated temperatures. Thus, the MD simulations demonstrated reduction of βPTH helicity at low and elevated temperatures in comparison with 300 K.

Thermal effects on structure and dynamics of each residue are presented in Fig. 2. A shift of temperature from ambient triggers large conformational changes in the α2 and both loops. The entire α2 helix shows large temperature dependant perturbations as indicated by the large bbRMSD and RMSF values. In contrast, the residues of the α1 are not significantly affected by changes in temperature as demonstrated by the relatively small bbRMSD and ahRMSD values. Remarkable thermal resistance of the α1 helix contributes to conformational

Fig. 2. Temperature-dependant changes in the structure and dynamics after the 1-ns simulations. (A) Time evolution of bbRMSD (in angstroms) between the MD trajectories at the temperatures of 280 K (gray line), 300 K (heavy black line), 360 K (dashed line), and 400 K (black line) and the crystal structure during the 1-ns simulations. (B–D) Effect of temperature on RMSD and RMSF (in angstroms) as functions of residue indices. (B) ahRMSD and (C) bbRMSD from the crystal structure and (D) RMSF for the MD trajectories at 280 K (dot-dashed line), 300 K (heavy continuous line), 360 K (dashed line), and 400 K (continuous line). The average values were calculated over the last 400 ps of 1-ns simulations. Schematic representation of the secondary structure as in Fig. 1E.

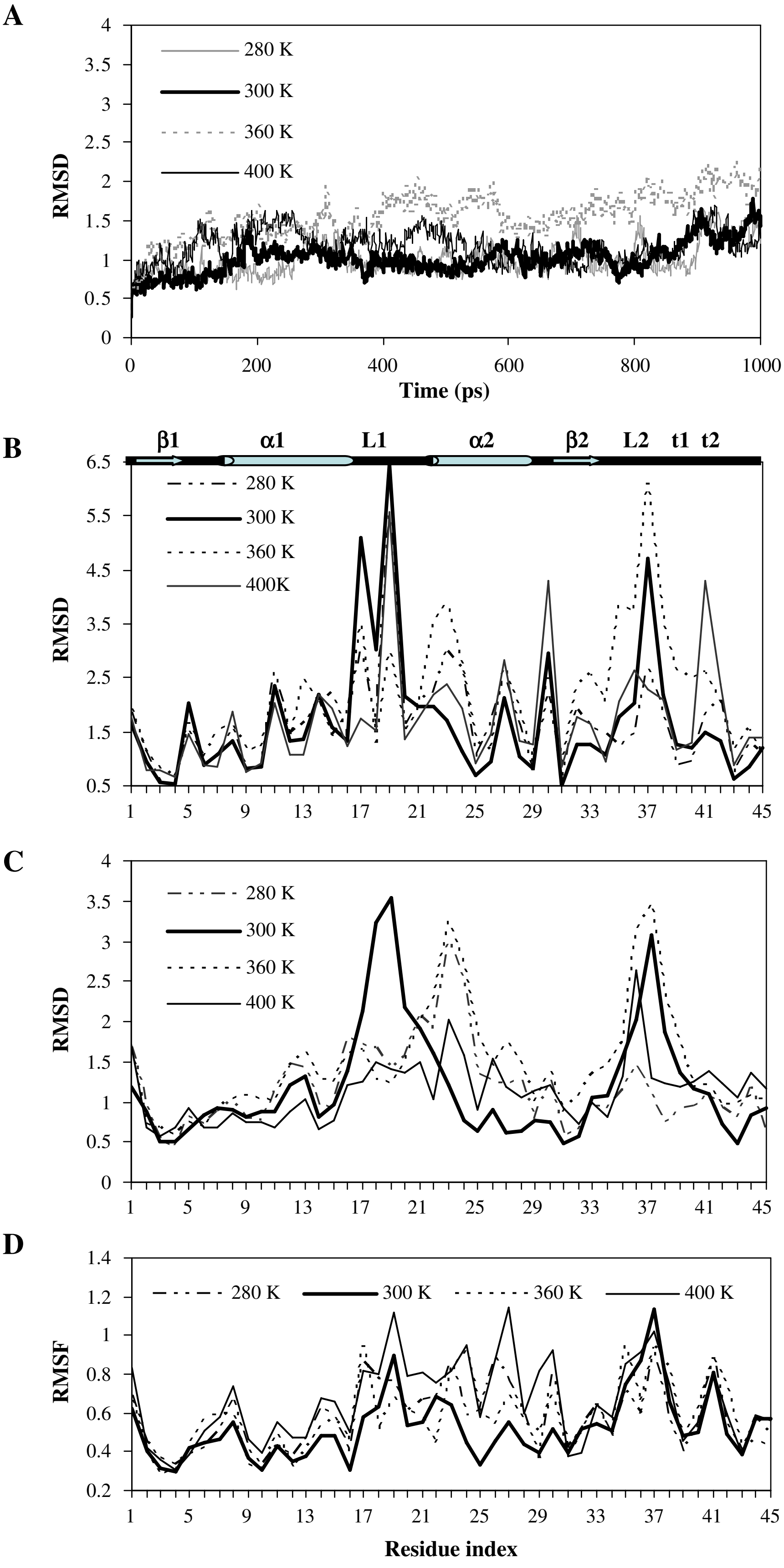
A
RMSD
280 K
300 K
360 K
400 K
0
0.5
1
1.5
2
2.5
3
3.5
4
0
200
400
600
800
1000
Time (ps)
B
β1
α1
L1
α2
β2
L2
t1
t2
RMSD
280 K
300 K
360 K
400K
0.5
1.5
2.5
3.5
4.5
5.5
6.5
1
5
9
13
17
21
25
29
33
37
41
45
C
RMSD
280 K
300 K
360 K
400 K
0
0.5
1
1.5
2
2.5
3
3.5
4
1
5
9
13
17
21
25
29
33
37
41
45
D
RMSF
280 K
300 K
360 K
400 K
0.2
0.4
0.6
0.8
1
1.2
1.4
1
5
9
13
17
21
25
29
33
37
41
45
Residue index

Table 2
Comparison of the secondary structure at different conditions

β-PTH	Conditions	α-helix	β-sheet	3-10 helix	Other
CrS[a]	300 K	0.38 (7–16, 22–28)[b]	0.13	0	0.49
MD	280 K	0.24 (7–17)	0.09	0.07 (16–18)	0.6
MD	300 K	0.38 (7–15, 22–29)	0.13	0.07 (22–24)	0.42
MD	360 K	0.22 (7–16)	0.13	0.07 (22–24)	0.58
MD	400 K	0.29 (7–19)	0.09	0.07 (22–24)	0.55
MD	300 K+K^+	0.38 (7–19, 26–29)	0.13	0.07 (22–24)	0.42
MD	300 K+Mg^{+2}	0.24 (7–17)	0.13	0.07 (22–24)	0.56

[a] Crystal structure [6].

[b] Residue indices forming a secondary structure are given in brackets.

stability of Tyr13. Both loops are very dynamic at all temperatures. Interestingly, the Arg30 ahRMSD values increase substantially only at 400 K despite large increases of the bbRMSD and RMSF values with a shift of temperature from ambient. This fact suggests the presence of conformational constraints for the Arg30 side chain in βPTH at temperatures below 400 K.

The SAA, computed for the whole peptide, increases at 360 K, but decreases at 400 K (see Supplementary material, Fig. 2). An exposure of the Tyr13 ring to the solvent is decreased at 400 K as indicated by the decreased SAA values, while the Arg30 SAA decreases at both elevated temperatures. Analyses of the hydrogen bonds confirm thermal stability of the Γ fold (Table 1). The hydrogen bonds between Lys45 and both Cys4 and Arg10 are retained in the range from 280 to 400 K. The outer hydrogen bond Arg10-NH1:Ser2-OG only is markedly weakened at the non-ambient temperatures. Shift of temperature from ambient in either direction perturbs the Asp42-Lys5-Arg30-Asn27 hydrogen bonding network where the Arg30-NH1: Asn27-O hydrogen bond is affected the most. These changes are consistent with unfolding of the α2 (Table 2).

Therefore, our data suggest an important role of Arg30 in decreasing helicity of βPTH. This finding is consistent with previous experiments that demonstrated a decrease of helicity for the D32R analog of the *P. pubera* thionin [7]. The D32R mutation results in reduction of helicity from 70% in the *P. pubera* thionin to 43% in the D32R analog. Arg32 in the D32R analog corresponds to Arg30 in βPTH which helicity is 35% in the βPTH-300K trajectory that explains similarity in helicity of these peptides. Due to similarity between the D32R analog and βPTH, we expected to find resemblance of thermal effects on βPTH with the analog rather than with the wild type. The helical pattern of the *P. pubera* thionin is preserved between 5 and 80 C°; however, helical pattern of the D32R analog is more thermally sensitive. Our simulations confirmed similarity between βPTH and the D32R analog by demonstrating reduction of βPTH helicity to 22–24% at 280 and 360 K (7 and 87 °C) in comparison with 300 K.

3.3. Effect of mono- and divalent metal ions

The 2-ns MD simulations were performed at 300 K in the presence of 100 mM KCl and 20 mM $MgCl_2$ to study K^+ and Mg^{2+}-dependent conformational changes of βPTH in water. Concentrations of metal ions used in the simulations were chosen to fully inhibit antimicrobial activity of βPTH according to experimental data [1,8]. The final ahRMSD from the crystal structure for the MD trajectories with K^+ (βPTH-K) and Mg^{2+} (βPTH-Mg) ions were 1.9 and 2.3 Å, respectively. The bbRMSD values did not differ significantly among all three trajectories during the second nanosecond even though the bbRMSD of the βPTH-Mg trajectory increased considerably between 600 and 900 ps (Fig. 3A). However, the superposition of the MD and the crystal structures displays substantial conformational changes triggered by the metal ions (Fig. 3B,C). Both metal ions trigger rearrangement in the entire α2 helix, elongate the α1 helix, and largely change conformation of the L1. Effects of K^+ and Mg^{2+} on secondary structures are presented in Table 2. During the runs, each Mg^{2+} ion becomes associated with a Cl^- ion and pentahydrated. All metal ions remain mobile and do not associate with any particular residue. This is consistent with experimental data because no particular binding site is found for Mg^{2+} ions in the βPTH crystal structure despite a high concentration of Mg^{2+} ions during crystallization [6].

Fig. 4 shows effects of metal ions on RMSD and RMSF values for each residue. Both cations have no significant effect on the α1 residues, but greatly increase the bbRMSD and ahRMSD values for the entire α2 helix that is analogous to the effects of temperature. Mg^{2+} ions induce greater conformational changes than K^+ in the α2 and also affect the β-sheet and the b-turns. Mobility of the L1 loop is largely reduced by both metal ions due to an extension of the α1 helix especially in the presence of Mg^{2+} ions. Mg^{2+} ions considerably reduce fluctuations in the L1 region in comparison with that of the βPTH-300K trajectory as well. Interactions with both cations largely constrain the Arg30 side chain close to the initial position. Mg^{2+}, but not K^+ ions, largely elevate the Arg30 fluctuating motions. These results show that metal ions and shift of temperature trigger similar conformational changes in the α-helical region although their effects on the peptide dynamics are different.

Comparison of the RMSF profiles for the βPTH-300K and βPTH-Mg trajectories with the temperature factor profile of βPTH demonstrates the effects of Mg^{2+} ions on peptide dynamics in the crystals. In particular, mobility of the L1 loop and the N-end of the α2 are reduced while mobility of Asn27, Arg30, and Lys32 are elevated in the βPTH-Mg in comparison with the βPTH-300K. As a result, the residues of the L1 fluctuate considerably less than Asn27 and Arg30, while Lys23, Asn27, and Arg30 display nearly the same level of mobility that is very similar to the dynamics described by the B factors in the βPTH crystals [6]. This fact can be explained when considering crystallization conditions because the βPTH crystals were obtained by equilibration against the buffer containing 20% $MgCl_2$. Consequently, the temperature factors reflect mobility of βPTH in the presence of Mg^{+2} ions. Therefore, our computations suggest that the Mg^{+2} ions in the inhibiting concentrations significantly alter dynamics of the peptide.

The SAA for all atoms and the side chain atoms of βPTH are not significantly affected in the presence of metal ions (see Supplementary material, Fig. 2). However, The SAA values for

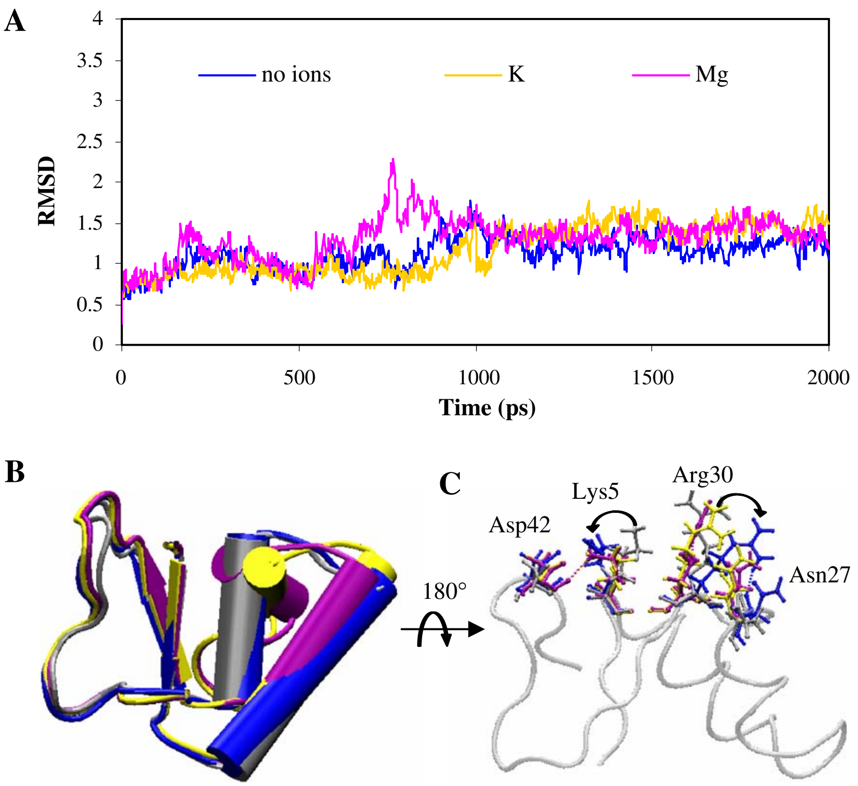

Fig. 3. Structural changes in the presence of 100 mM K^+ and 20 mM Mg^{2+} ions after the 2-ns MD simulations at 300 K. (A) Time evolution of bbRMSD (in angstroms) between the MD trajectories with no metal ions present (blue line), with 100 mM K^+ (yellow line), and with Mg^{2+} ions (purple line) and the crystal structure during the 2-ns simulations. (B) Superposition of the averaged MD structures with K^+ (yellow), Mg $^{2+}$ (purple), and no metal ions added (blue) with the crystal structure (gray). Structures were averaged over the last nanosecond. (C) The Asp42-Lys5-Arg30-Asn27 interacting group in the superposed MD structures is shown. The structures are colored as in (B).

conserved residues Tyr13 and Arg30 are reduced in the βPTH-K and βPTH-Mg trajectories. Thus, we found that both metal ions reduce exposure of the Tyr13 ring to the solvent. This is consistent with previous experiments showing that presence of divalent metal ions modifies a steric environment of Tyr13 [9,10]. Both metal ions cause a strengthening of the hydrogen bonds forming the Γ fold especially the hydrogen bonding between the C terminus and Arg10 (Table 1). The Γ fold becomes consequently more rigid that is consistent with the reduced exposure of Tyr13 to the solvent. Importantly, addition of K^+ and Mg^{2+} ions alters the Asp42-Lys5-Arg30-Asn27 network by stronger hydrogen bonding interactions of Lys5 with Asp42 and of Arg30 with Asn27.

Electrostatic effects can substantially alter pK_a values in a protein environment. To examine effects of K^+ and Mg^{2+} ions on protonation states of the ionizable residues, we performed continuum dielectric calculations on the MD trajectories with and without metal ions added. The pK_a calculations indicate that Mg^{2+} ions only significantly reduce positive charge on the peptide especially affecting Arg30. The intrinsic pK_a shifts are presented in Fig. 5. K^+ and Mg^{2+} ions produce different effects on pK_a of the ionizable residues. The pK_a shifts are negative for the majority of the ionizable residues in the βPTH-Mg structure. Our calculations predicted that Lys1 and Arg19 become partially charged. The residues located on the opposite ends of the α2 helical dipole undergo the largest pK_a shifts. Arg30, located at the C-end of the helical dipole, displays a negative shift of −78 while Lys23 located at the N-end displays a four-fold lesser positive shift in the presence of Mg^{+2} ions. Therefore, Arg30 is likely to be deprotonated at neutral pH in the βPTH-Mg trajectory. In contrast, K^+ ions induce a significant negative shift of pKa of the C-terminus and increase the pK_a of Arg19 and Lys32 making them likely to be protonated at neutral pH. No significant shift of pK_a of Arg30 and Lys23 occurs in the βPTH-K trajectory. Note that all explicit ions were removed from the MD trajectories for pK_a calculations, and, hence, the obtained pK_a shifts are a result of conformational changes in the peptide induced by the metal ions.

To better understand effects of K^+ and Mg^{2+} ions on electrostatics of βPTH, we calculated the electrostatic potential by solving the Poisson equation. The electrostatic potential in the βPTH-K and βPTH-Mg structures is changed considerably compared to βPTH-300K potential especially in the corner of the Γ fold and the α-helical region (data not shown). The wide hydrophilic belt running through the Γ fold and the middle of the stem observed in the βPTH-300K structure becomes interrupted due to conformational changes in the α2. Electrostatic interactions of βPTH with the membrane are important for membrane permeabilizing activity. Strong electrostatic interactions of βPTH with lipid headgroups were demonstrated during insertion of the peptide into the membrane [4,5]. Modification

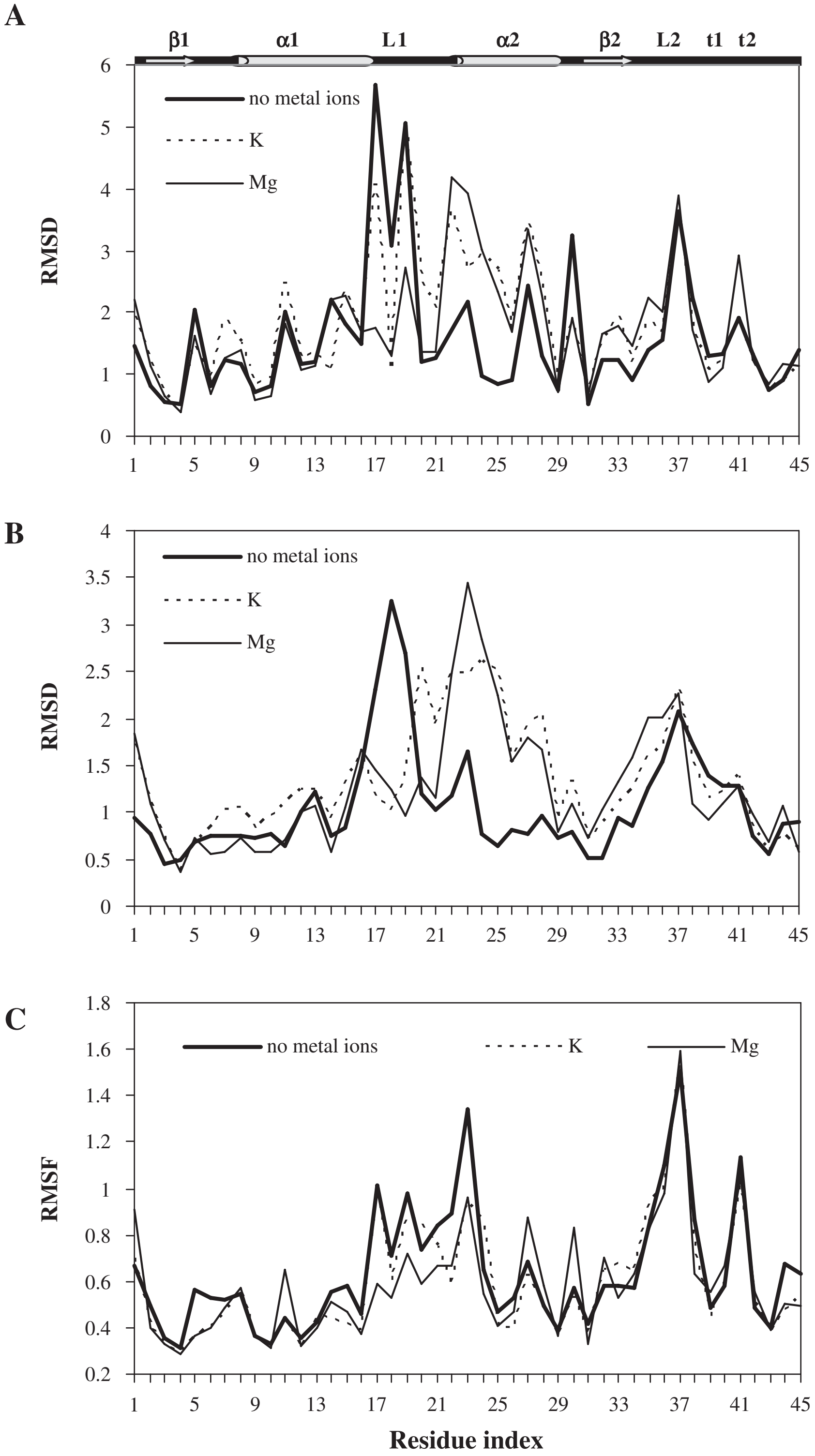

Fig. 4. Effects of K^+ and Mg^{2+} ions at 300 K on RMSD and RMSF (in angstroms) as functions of residue indices. (A) ahRMSD and (B) bbRMSD between the MD and the crystal structures and (C) RMSF for the MD trajectories without metal ions (heavy continuous line), with 100 mM of K^+ (dashed line), and with 20 mM Mg^{2+} (continuous line). The average values were calculated over the last nanosecond of 2-ns simulations. Schematic representation of the secondary structure as in Fig. 1E.

of the βPTH electrostatic potential could contribute to inhibiting βPTH membrane permeabilizing activity by mono- and divalent metal ions.

Therefore, our MD simulations demonstrate that mono- and divalent metal ions trigger the large conformational changes in the helical region that explains loss of βPTH toxicity. Rigidity of the Γ fold modifying a Tyr13 steric environment and of the L1 loop can contribute to inability of the peptide to permeabilize membranes. Screening of ionic interactions between the thionins and the lipid headgroups was previously suggested as

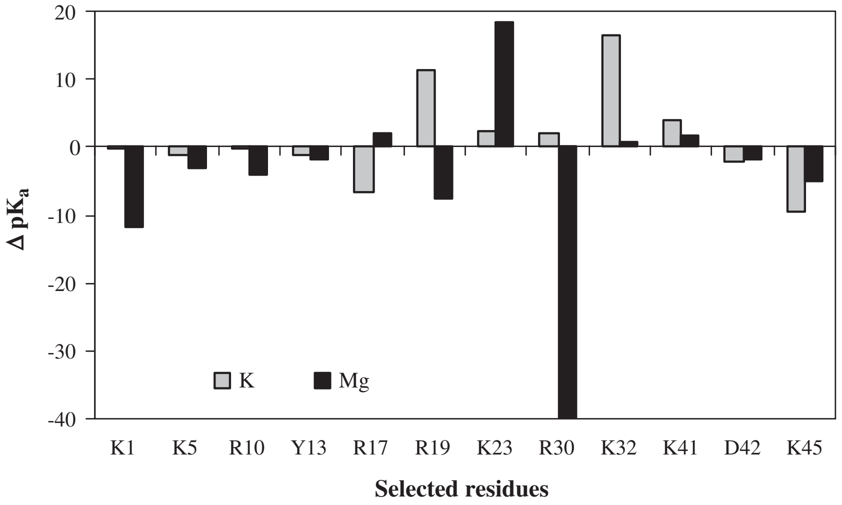

Fig. 5. pK$_a$ shifts in the presence of K^+ and Mg^{2+} ions for the selected ionizable residues. The ΔpK$_a$ were calculated as differences between the pK$_a$ calculated for the residues in the averaged MD structures with cations and with no cations added. ΔpK$_a$ for K^+ ions (gray) and for Mg^{2+} ions (black).

the mechanism of inhibition for monovalent ions [40]. Divalent ions were suggested to chelate the thionin binding sites [8]. Our findings are consistent with the fact that the metal ion inhibition is not reversed by chelation [8] unlike the above mentioned hypotheses.

3.4. Instability of the α2 helix

The MD simulations demonstrated sensitivity of the α2 helix to environmental conditions such as temperature and the presence of metal ions. The intact α2 was in fact observed only at 300 K with no metal ions added. In contrast, the α1 was stable in all MD simulations. To understand the nature of discrepancy in stability between the α1 and α2, the time evolution of secondary structures in the presence of metal ions was investigated. The α2 unfolded after 800 ps starting at the C-end in both, the βPTH-K and the βPTH-Mg trajectory. In the βPTH-K trajectory, unfolding occurred slowly so the N-terminal part remained intact during next 100 ps. In the βPTH-Mg trajectory, the α2 unfolded rapidly with the N-terminus forming a 3-10-helix.

To study the conformational transition of the α2 helix, the time evolution of the dihedral angles and side-chain conformations of the α2 and linked regions were analyzed. The major differences between the βPTH-300K, βPTH-K, and βPTH-Mg trajectories within first 800 ps are found for the φ and ψ backbone dihedral angles of Arg30, Val28, and Asn27 (Fig. 6). The φ and ψ of these residues exist in the predominant and the transient conformations that indicate increased flexibility of their backbones. Arg30 has the most flexible backbone with the predominant and the transient (φ,ψ) values of (80°,50°) and (80°,0°), respectively. Val28 and Asn27 exist predominantly in the (−70°,−10°) and the (−70°, −50°) conformations, respectively. Mg^{+2} ions considerably modify the backbone conformations of all three residues early in the simulation. During the first 800 ps, the Arg30 ψ angle gradually decreases to 0°, assuming the (80°,0°) conformation which is transient in the βPTH-300K trajectory, and then returns to 50° which is predominant in the βPTH-300K. The Val28 φ angle undergoes the similar arch-like changes. The Asn27 φ angle twice switches from −70° to −110° at 200 and 700 ps. The backbones of other residues in the α2 and the linked regions are stable and not affected by metal ions during the first 800 ps. K^+ ions induce conformational changes starting from 800 ps modifying the Arg30 φ, Val28 φ, and Asn27 ψ values (data not shown).

The side-chain conformations were compared to the backbone-dependent (BBD) library [41]. The BBD describes a range of possible values for the χ_1 rotamers which are very sensitive to the values of the φ and ψ dihedral angles. Fig. 6 gives the φ, ψ, and χ_1 angles of Lys5, Asn27, Val28, and Arg30 during the MD simulations without and with Mg^{+2} ions. The Arg30 χ_1 rotamer found in the βPTH-300K trajectory explores two conformations with the (φ,ψ,χ_1) values at (80°,0°,60°) and (80°,50°,70°) which have zero probabilities according to the BBD library. The Arg30 χ_1 rotamers in the βPTH-K and βPTH-Mg trajectories assume several conformations which are unusual as well. The Val28 χ_1 rotamer in the βPTH-300K trajectory starts from the rear conformation (−120°,−10°,60°) but assumes the more populated conformation (−70°,−10°,60°) after 200 ps. In the βPTH-Mg trajectory, the Val28 χ_1 rotamer explores mainly the conformations with low probabilities. The Asn27, Cys25, Lsy23 χ_1 rotamers change to less probable conformations in the presence of metal ions as well. However, the Lys5 side chain changes conformation from the unpopulated χ_1 rotamer in βPTH-300K trajectory to the highly probable rotamers in the presence of both metal ions. The other residues of the α2 helix and the linked regions sample the highly probable χ_1 rotamers in the trajectories without and with metal ions.

Thus, Arg30 is maintained in the unusual conformation in βPTH and is associated with unfolding of the α2 [7]. This finding is in an excellent agreement with the experimental data. An important role of Arg located at the C-end of the α2 in decreasing helicity was demonstrated previously for the *P. pubera* thionin. The lower helical content observed in the D32R

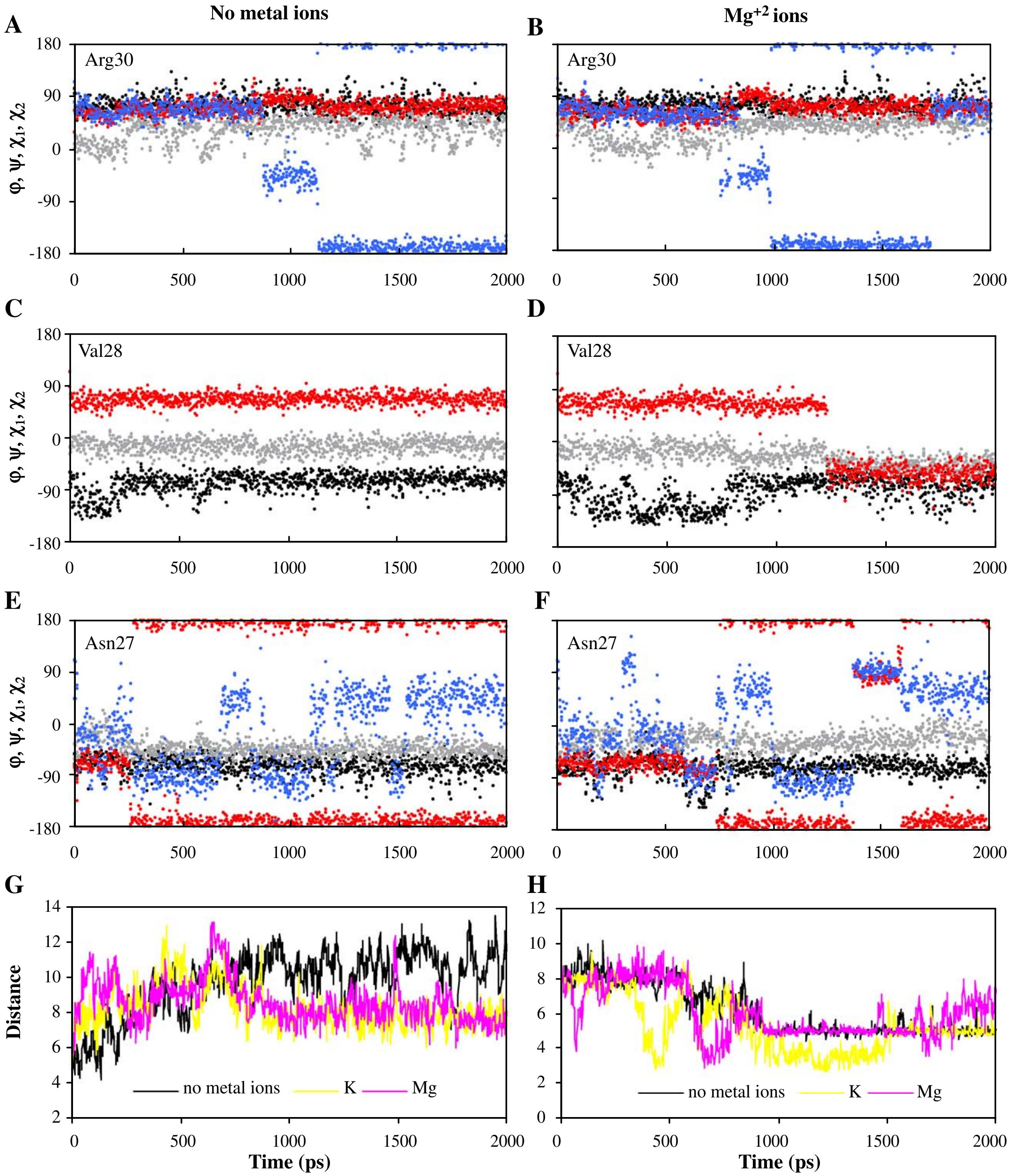

Fig. 6. Conformational changes associated with unfolding of the α2 helix. (A–F) φ (black dots) with ψ (gray dots) represent backbone dihedral angles, and χ_1 (red dots) with χ_2 (blue dots) represent side-chain dihedral angle values of residues (A, B) Arg30, (C, D) Val28, and (E, F) Asn27 in the MD trajectories (left graphs) without metal ions and (right graphs) with 20 mM Mg^{+2} ions. (G) Distance (in angstroms) between the Lys5 NZ atom and the Arg30 NE atom and (H) between the Arg30 NH2 atom and the Asn27 O atom.

analog was suggested to result from the repulsive interactions between Lys29 and Arg32 in the i and $i+3$ positions, respectively. In βPTH, both α-helices contain residues Asn and Arg (i, $i+3$ position) at the C-end, Asn14 with Arg17, and Asn27 with Arg30, respectively; however, they differ greatly in stability.

The main difference between the α1 and the α2 C-terminus consists of the strong linkage of two positively charged residues Arg30 and Lys5 by the disulfide bonds at the α2 C-end. Our results indicate that interactions between Arg30 and Lys5 cause sensitivity of the α2 to environmental conditions. In the βPTH-300K trajectory, the initial interaction energy between Arg30 and Lys5 is high indicating strong repulsive interactions (Fig. 7A). Then, the interaction energy reduces nearly two-fold during the first 800 ps while the distance between the Lys5 NZ and Arg30 NE atoms gradually increases from 4 to 11 Å (Fig. 6G). In contrast, the interaction energy in the presence of metal ions is reduced considerably in comparison with the βPTH-300K during the first 200 ps. The distance between the Lys5 NZ and the Arg30 NE atoms fluctuates considerably and then drops to 8 Å around 800 ps when unfolding of the α2 begins. The averaged interaction energy calculated over the second nanosecond is significantly larger in the presence of metal ions than in the βPTH-300K trajectory (Fig. 7B).

Therefore, the distance between the Lys5 and Arg30 side chains is maximized and the interaction energy between Arg30 and Lys5 is minimized in the βPTH-300K trajectory. As a result, the Arg30 side chain is stable, the Arg30 backbone does not undergo conformational perturbations, and the α2 remains intact. We suggest that stabilization of the Arg30 side chain occurs due to repulsive interactions between Lys5 and Arg30 directing both side chains away from each other (Fig. 3C), maximizing distance and minimizing repulsive interactions between the positively charged residues. Lys5 forms a hydrogen bonding with Asp42, and Arg30 forms a Arg30-NH1:Asn27-O hydrogen bond. These coupled hydrogen bonding interactions stabilize the Arg30 side chain.

The metal ions alter interactions between Arg30 and Lys5 resulting in perturbation of the α2 C-end. Both metal ions screen repulsive interactions between Arg30 and Lys5. Consequently, no directed movement of the Agr30 side chain in opposite direction from Lys5 is observed. Instead, the Arg30 side chain flaps in different directions that causes perturbations in the Agr30 backbone atoms and further in the Val28 backbone atoms. In addition, the destabilized Arg30 side chain periodically interacts with the Asn27 O atom, aiding in disrupting the α2 C-end. Fig. 6H shows the decrease in distance between the Arg30NH2 and Asn27O atoms nearly at 100 and 600 ps in the βPTH-Mg trajectories. The Asn27 backbone undergoes conformational perturbation at the same time (Fig. 6F). Perturbation of the C-end causes rearrangement of the entire α2.

4. Conclusions

Using unconstrained MD simulations performed with the simulation parameters optimized to achieve reliable computational accuracy, we obtained computational results which reproduced several experimental data. This fact demonstrates the adequate representation of βPTH in our model system and the reliability of computationally predicted properties. In particular, we demonstrated the temperature dependent decrease of the βPTH helicity that is in agreement with the previously reported thermal effects on the D32R analog of the *P. pubera* thionin [7]. We showed that the 20 mM Mg^{+2} induces larger structural and dynamic changes than the 100 mM K^+ that is in agreement with the experimental data where 5- to 10-fold larger concentrations of monovalent metal ions were necessary to inhibit thionins in comparison with divalent ions [1,42]. Our MD simulations reproduced modification of a steric environment of Tyr13 by the presence of metal ions [9,10]. Finally, the βPTH-Mg trajectory displayed effects of Mg^{+2} ions on the peptide dynamics similar to those observed in the βPTH crystals obtained in the presence of 20% $MgCl_2$ [6]. Consistency between computational and experimental results strongly indicates high accuracy of our MD calculations which allowed us to correctly capture properties of the model biomolecule. Structural and dynamic details obtained by these simulations are not available experimentally, and, therefore, provide valuable contribution for understanding βPTH properties as well as the mechanism of the metal ion inhibition.

Comparison of the MD trajectories at different temperatures and in the presence of K^+ and Mg^{+2} provides insights into the key properties of βPTH. The global Γ fold and the α1 helix are resistant to changes of temperature and presence of K^+ and Mg^{+2}. These structures stabilize conformation of the Tyr13 ring in the peptide core. In contrast, the α2 helix is sensitive to both shift of temperature from ambient and the presence of metal ions. The most sensitive is the C-end of the α2 which unfolds in response to the environmental changes. Formation of the Asp42-Lys5-Arg30-Asn27 hydrogen bonding cluster is important for maintaining the intact α2 helix in water. Our results indicate that the Asp42-Lys5-Arg30-Asn27 hydrogen bonding

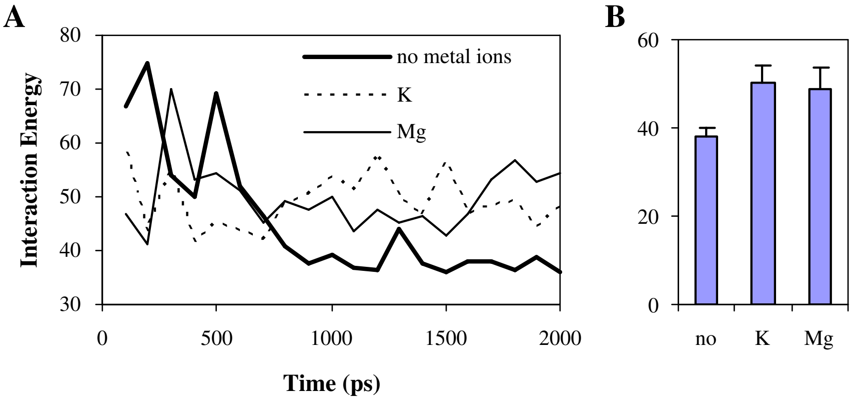

Fig. 7. Interaction energy (in kilocalories per mole) between the residues Lys5 and Arg30. (A) Time evolution of interaction energy in the MD trajectories with no metal ions (heavy continuous line), K^+ ions (dashed line), and Mg^{2+} ions (continuous line). (B) Average values with standard deviations of interaction energy in the MD trajectories with no metal ions (no), K^+ ions (K), and Mg^{2+} ions (Mg) computed over the last nanosecond.

network, which is not found in the crystal structure stabilizes the Arg30 side chain minimizing repulsive interactions between Arg30 and Lys5. Notably, the highly conserved residues maintain this cluster and, therefore, sensitivity of the α2 C-end to environmental changes. A shift of temperature and the addition of metal ions alter interactions between Lys5 and Arg30 and trigger large conformational perturbations in the entire α2. Loop regions display high flexibility and elevated dynamics at all temperatures tested. However, the L1 loop as well as the Γ fold become more rigid in the presence of metal ions as compared to those when no metal ions added [6].

Structural and dynamic details found in this work increase our understanding of inhibition of βPTH membrane permeabilizing capability by metal ions. Addition of K^+ and Mg^{2+} ions in the concentrations inhibiting antimicrobial activity induces large conformational changes in the α2 helix, altering the hydrophobic region between the α-helices. As a result, the wide hydrophilic belt running through the Γ fold and the middle of the stem observed in the intact peptide becomes interrupted. Mg^{2+} ions cause larger structural and dynamic changes than K^+ ions and greatly reduce the pK_a of Arg30. Unfolding of the α2 is triggered by altering interactions between Lys5 and Arg30. The Arg30 side chain becomes destabilized causing conformational perturbations in the Arg30 and Asn27 backbone atoms that trigger unfolding of the α2 helix. Reduced plasticity of the Γ fold that modifies a Tyr13 steric environment could contribute to inhibiting effects of metal ions as well.

Acknowledgments

This work was supported by LSU AgCenter Experiment Station. Simulations were performed at LSU's Center for Applied Information Technology and Learning (CAPITAL) and Biological Computation and Visualization Center (BCVC).

Appendix A. Supplementary materials

Supplementary data associated with this article can be found, in the online version, at doi:10.1016/j.bpc.2005.12.004.

References

[1] K. Thevissen, F. Terras, W.F. Broekaert, Permeability of fungal membranes by plant defensins inhibits fungal growth, Appl. Env. Microbiol. 63 (1999) 5451–5458.

[2] F. Garcia-Olmedo, A. Molina, J.M. Alamillo, P. Rodriguez-Palenzuela, Plant defense peptides, Biopolymers 47 (1998) 479–491.

[3] S. Oard, M.C. Rush, J.H. Oard, Characterization of antimicrobial peptides against a US strain of the rice pathogen *Rhizoctonia solani*, J. Appl. Microbiol. 97 (2004) 169–180.

[4] J.-A. Richard, I. Kelly, D. Marion, M. Pezolet, M. Auger, Interaction between β-purothionin and dimyristoylphosphatidylglycerol: a ^{31}P-NMR and infrared spectroscopic study, Biophys. J. 83 (2002) 2074–2083.

[5] B. Stec, O. Markman, U. Rao, G. Heffron, S. Henderson, L.P. Vernon, V. Brumfeld, M.M. Teeter, Proposal for molecular mechanism of thionins deduced from physicochemical studies of plant toxins, J. Pept. Res. 64 (2004) 210–224.

[6] B. Stec, U. Rao, M.M. Teeter, Refinement of purothionins reveals solute particles important for lattice formation and toxicity: Part 2. Structure of beta-purothionin at 1.7 angstroms resolution, Acta Crystallogr., D Biol. Crystallogr. 51 (1995) 914–924.

[7] M. Vila-Perello, A. Sanchez-Vallet, F. Garcia-Olmedo, A. Molina, D. Andreu, Synthetic and structural studies on *Pyrularia pubera* thionin: a single-residue mutation enhances activity against Gram-negative bacteria, FEBS Lett. 536 (2003) 215–219.

[8] P. Hughes, E. Dennis, M. Whitecross, D. Llewellyn, P. Gage, The cytotoxic plant protein, b-purothionin, forms ion channels in lipid membranes, J. Biol. Chem. 275 (2000) 823–927.

[9] W. Fracki, D. Li, N. Owen, C. Perry, G. Naisbitt, L. Vernon, Role of Tyr and Trp in membrane responses of *Pyrularia* thionin determined by optical and NMR spectra following Tyr iodination and Trp modification, Toxicon 30 (1992) 1427–1440.

[10] K. Wada, Y. Ozaki, H. Matsubara, H. Yoshizumi, Studies on purothionin by chemical modifications, J. Biochem. 91 (1982) 257–263.

[11] S. Van Campenhout, L. S., J. Vander Stappen, G. Vlockaert, Characterisation of type-I thionin loci from the A, B, D, and R genomes of wheat and rye, Theor. Appl. Genet. 96 (1998) 80–86.

[12] H. Gao, Y. Kong, Simulation of DNA–nanotube interactions, Annu. Rev. Mater. Res. 34 (2004) 123–150.

[13] C.M. Niemeyer, Nanoparticles, proteins and nucleic acids: biotechnology meets materials science, Angew. Chem., Int. Ed. Engl. 40 (2001) 4128–4158.

[14] W. Wang, O. Donini, C.M. Reyes, P.A. Kollman, Biomolecular simulations: recent developments in force fields, simulations of enzyme catalysis, protein–ligand, protein–protein, and protein–nucleic acid noncovalent interactions, Annu. Rev. Biophys. Biomol. Struct. 30 (2001) 211–243.

[15] R. Varekova, J. Koca, C. Zang, Complexity and convergence of electrostatic and van der Waals energies within PME and cutoff methods, Int. J. Mol. Sci. 5 (2004) 154–173.

[16] C. Sagui, T.A. Darden, Molecular dynamics simulations of biomolecules: long-range electrostatic effects, Annu. Rev. Biophys. Biomol. Struct. 28 (1999) 155–179.

[17] R.M. Levy, E. Gallicchio, Computer simulations with explicit solvent: recent progress in the thermodynamic decomposition of free energies and in modeling electrostatic effects, Annu. Rev. Phys. Chem. 49 (1998) 531–567.

[18] Y. Komeiji, M. Uebayasi, Peach–Grape system — a high performance simulator for biomolecules, Chem-Bio Info. J. 2 (2002) 102–118.

[19] L.X. Dang, B.M. Pettitt, Solvated chloride-ions at contact, J. Chem. Phys. 86 (1987) 6560–6561.

[20] O. Teleman, B. Jonsson, S. Engstrom, A molecular dynamics simulations of a water model with intramolecular degree of freedom, Mol. Phys. 60 (1987) 193–203.

[21] J. Wang, P. Cieplak, P.A. Kollman, How well does a restrained electrostatic potential (RESP) model perform in calculating conformational energies of organic and biological molecules? J. Comput. Chem. 21 (2000) 1049–1074.

[22] Y. Komeiji, Y. Uebayasi, R. Takata, A. Shimizu, K. Itsukashi, M. Taiji, Fast and accurate molecular dynamics simulation of a protein using a special-purpose computer, J. Comput. Chem. 18 (1997) 1546–1563.

[23] Y. Komeiji, M. Uebayasi, Change in conformation by DNA-peptide association: molecular dynamics of the Hin-recombinase–hixL complex, Biophys. J. 77 (1999) 123–138.

[24] W.G. Hoover, Canonical dynamics: equilibrium phase–space distributions, Phys. Rev., A 31 (1985) 1695–1697.

[25] S. Nose, A unified formulation of the constant temperature molecular dynamics methods, J. Chem. Phys. 81 (1984) 511–519.

[26] T. Darden, D. York, L. Pedersen, Particle mesh Ewald: an N.log(N) method for Ewald sums in large systems, J. Chem. Phys. 98 (1993) 10089–10092.

[27] T. Nemoto, M. Uebayasi, Y. Komeiji, Flexibility of a loop in a pheromone binding protein from *Bombyx mori*: a molecular dynamics simulation, Chem-Bio Info. J. 2 (2002) 32–37.

[28] S. Vemparala, B.B. Karki, R.K. Kalia, A. Nakano, P. Vashishta, Large-scale molecular dynamics simulations of alkanethiol self-assembled monolayers, J. Chem. Phys. 121 (2004) 4323–4330.

[29] D.A. Pearlman, D.A. Case, J.W. Caldwell, W.R. Ross, I.T.E. Cheatham, S. DeBolt, D. Ferguson, G. Seibel, P.A. Kollman, AMBER, a computer

program for applying molecular mechanics, normal mode analysis, molecular dynamics and free energy calculations to elucidate the structures and energies of molecules, Comput. Phys. Commun. 91 (1995) 1–41.

[30] W. Kabsch, C. Sander, Dictionary of protein secondary structure: pattern recognition of hydrogen-bonded and geometrical features, Biopolymers 22 (1983) 2577–2637.

[31] D.A. Humphrey W, Schulten K., VMD: visual molecular dynamics, J. Mol. Graph., 14 (1996) 33–38, 27–38.

[32] R. Koradi, M. Billeter, K. Wuthrich, MOLMOL: a program for display and analysis of mactomolecular structures, J. Mol. Graph. 14 (1996) 51–55.

[33] E. Demchuk, R.C. Wade, Improving the continuum dielectric approach to calculating pK_as of ionizable groups in proteins, J. Phys. Chem. 100 (1996) 17373–17387.

[34] A. Kahyaoglu, F. Jordan, Direct proton magnetic resonance determination of the pKa of the active center histidine in thiolsubtilisin, Protein Sci. 11 (2002) 965–973.

[35] J.-H. Lin, N.A. Baker, J.A. Mc-Cammon, Bridging implicit and explicit solvent approaches for membrane electrostatics, Biophys. J. 83 (2002) 1374–1379.

[36] M. Tada, Y. Kobashigawa, M. Mizuguchi, K. Miura, T. Kouno, Y. Kumaki, M. Demura, K. Nitta, K. Kawano, Stabilization of protein by replacement of a fluctuating loop: structural analysis of a chimera of bovine alpha-lactalbumin and equine lysozyme, Biochemistry 41 (2002) 13807–13813.

[37] J.W. Pitera, W. Swope, Understanding folding and desing: replica-exchange simulations of "Trp-cage" miniproteins, Proc. Natl. Acad. Sci. 100 (2003) 7587–7592.

[38] K. Adechi, E. Saiz, E. Riande, Molecular dynamics simulations of the dielectric relaxation behavior of polymers and their solutions at high temperatures, Phys. Chem. Chem. Phys. 4 (2002) 635–640.

[39] S. Jang, E. Kim, S. Shin, Y. Pak, Ab initio folding of helix bundle proteins using molecular dynamics simulations. J. Am. Chem. Soc. 125 (2003) 14841–14846.

[40] L.P. Vernon, A. Rogers, Binding properties of *Pyrularia thionin* and *Naja naja kaouthia* cardiotoxin to human and animal erythrocytes and to murine P388 cells, Toxicon 30 (1992) 711–721.

[41] R.L. Dunbrack Jr., F.E. Cohen, Bayesian statistical analysis of protein side-chain rotamer preferences, Protein Sci. 6 (1997) 1661–1681.

[42] M. Berrocal-Lobo, A. Segura, M. Moreno, G. Lopez, F. Garcia-Olmedo, A. Molina, Snakin-2, an antimicrobial peptide from potato whose gene is locally induced by wounding and responds to pathogen infection, Plant Physiol. 128 (2002) 951–961.